ISTFA 2008: Proceedings from the 34th International Symposium for Testing and Failure Analysis
November 2-6, 2008, Portland, Oregon USA
Copyright © 2008 ASM International®
All rights reserved.
DOI: 10.1361/cp2008istfa320

Applications of *In-situ* Sample Preparation and Modeling of SEM-STEM Imaging

R.J. Young, A. Buxbaum, B. Peterson
FEI Company, Hillsboro, Oregon, USA

R. Schampers
FEI Company, Eindhoven, The Netherlands

Abstract

Scanning transmission electron microscopy with scanning electron microscopes (SEM-STEM) has become increasing used in both SEM and dual-beam focused ion beam (FIB)-SEM systems. This paper describes modeling undertaken to simulate the contrast seen in such images. Such modeling provides the ability to help understand and optimize imaging conditions and also support improved sample preparation techniques.

Introduction

The dual-beam (FIB/SEM) offers the capability of both highly localized sample preparation and high-resolution sample analysis. Site-specific cross-sections and S/TEM samples of disparate materials can be prepared using FIB milling, while the SEM can be used to monitor the sample preparation, allowing the section to be precisely positioned [1-3]. Using a SEM-STEM detector in the dual-beam with a thin sample adds the capability for high-contrast, high-resolution imaging, providing complementary image information to standard SEM imaging. By mounting the sample on a pivoting sub-stage (a “flipstage”) it is possible to orient the sample for FIB thinning and then to position it for SEM-STEM imaging without breaking vacuum, enabling fast inspection of the thinned sample and even direct monitoring of the thinning process [4,5].

This paper describes modeling undertaken to understand better the expected contrasts seen in the various SEM-STEM modes and how they change with imaging conditions, such as, sample thickness, electron beam voltage and different material parameters. Such modeling can help interpret the contrast seen within the SEM-STEM images and help optimize sample preparation and imaging conditions.

Motivation for Modeling

SEM-STEM detectors are available for many different types of SEM and dual-beam FIB/SEM instruments, including systems that use full wafers as well as those that handle wafer pieces and packaged parts [3-8], Fig. 1. Such STEM detectors add the capability for high-contrast, high-resolution imaging at <0.8 nm resolution. The operation of the various STEM detectors is similar, although the sample-detector geometries and signal detection methods vary.

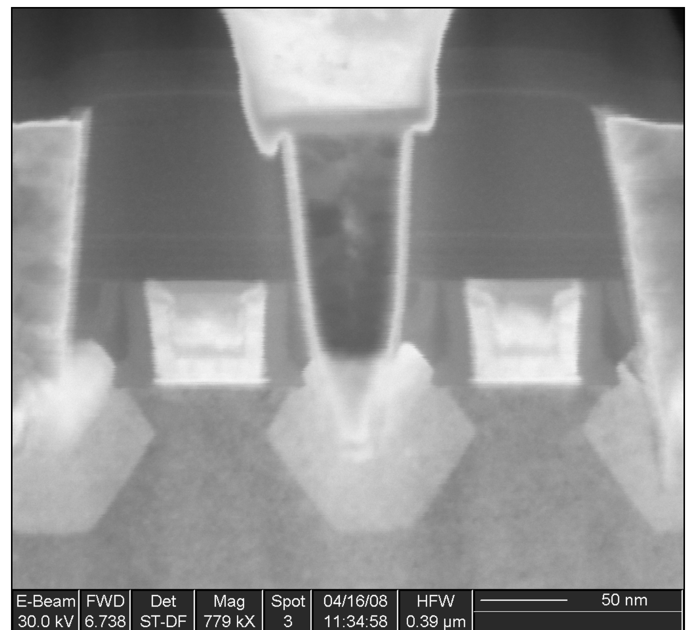

Figure 1: 45 nm node transistors imaged on a full 300 mm dual-beam FIB/SEM. Image is annular dark field STEM, with field of view of 390 nm.

The STEM detector is placed some distance below a thin sample, enabling transmitted electrons to be detected using, for example, a solid state diode similar to those used in back scatter electron detectors. The detectors are often divided up into a number of separate regions that can each be used alone

or with other regions to form the final image. Bright field (BF) images are formed from electrons that exit the sample directly below the incident beam, while dark field images (ADF – annular dark field; and HADF – high angle dark field) are formed from more scattered electrons, Fig. 2. In addition, in the detectors considered here the HADF region is broken into 12 sub-segments (like a clock-face), enabling collection of signal from either the full annular region, or just a fraction of it.

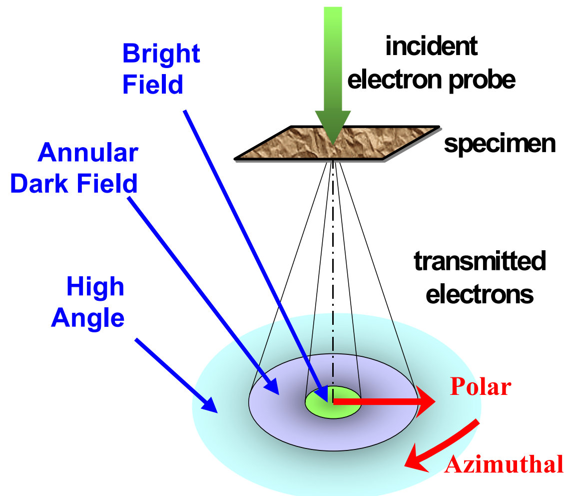

Figure 2: Schematic representation of STEM process. See text for a discussion of the polar and azimuthal angular directions.

The interaction of the beam with the sample results in a series of scattering events and other interactions that produces a transmitted beam with some angular distribution of intensity in both the polar (angle to the incident beam) and azimuthal (angle in the plane of the detector) directions (see labels in Fig. 2). The azimuthal angular variation mainly comes into play when considering interfaces between materials, but for a uniform amorphous material it can be ignored and only the polar variation considered.

To date the authors are not aware of a systematic study of the contrast mechanisms in these samples, and the modeling discussed here is designed to give a better understanding of how the different images are formed, and how images can be optimized whether in terms of sample thickness, beam voltage or detector design/geometry.

Monte-Carlo Simulations

The initial study was carried out using a Monte-Carlo modeling program to simulate how the incoming electrons interacted with various materials and sample thicknesses. The program used for the study is "MC-SET" [9], Fig. 3. This program allows the trajectory of the transmitted electrons to be tracked based on data in the log file created. An experiment is set up with a sample of a given thickness and set of materials. The program allows one parameter to be varied to create a series of result files, for example beam position or beam energy.

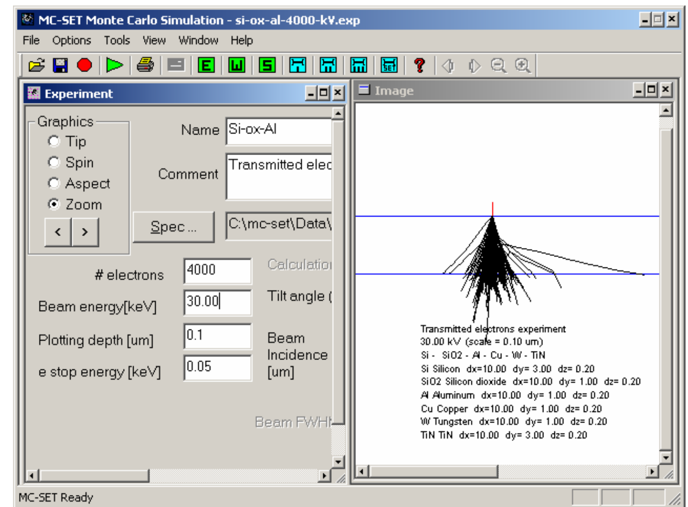

Figure 3: Screen shot from the "MC-SET" Monte-Carlo simulation program used for this study. In the example shown, 4000 electrons at 30 kV interact with a 200 nm thick sample. Only one of the materials making up the sample is shown due to the zoom level.

Each region in a sample is characterized by atomic number (Z), atomic weight (A) and density (D) (g/cm^2). This data is normally straightforward for elements, but for compounds there are several methods for how to combine the various A and Z values to give aggregate values for the region. The two main methods to calculate the aggregate A and Z are weighting the values based on number (atomic) fraction or by weight fraction. Which method to use for general Monte Carlo experiments seems to vary by application, and sometimes one is used for Z and one for A. For these tests, the weight fraction method was generally employed. Also, the density value for a compound may not be well known, or could be different from the typical bulk value due to the method of deposition. In addition, the Monte-Carlo modeling treats the material as amorphous, so crystalline effects have not been considered in the current modeling.

For each experiment MC-SET creates a series of data files that include information on electron trajectory through the samples and transmitted and backscattered electrons. X-rays can also be modeled, but this data has not been considered so far. The transmitted data files were imported and analyzed by a series of scripts that enables the angle of each electron relative to the incident beam to be calculated. The angular distribution of electrons can then be combined with knowledge of the sample-to-detector spacing and the detector geometry to calculate which part of the detector the electron will hit, and therefore which type of image (BF, ADF, HADF) the electron will contribute to. For some lens conditions, the magnetic immersion field also needs to be taken into account as this will change the effective angle of electrons that are collected by each detector segment.

A histogram of these polar angles in 1 degree increments is the result for each set of conditions. The signal for a particular detector configuration can then be calculated from this histogram by summing up the appropriate angular contributions. It is also possible to calculate the azimuthal angle so that signals into different sectors of a high-angle dark field detector can be considered. This was investigated for a SiO_2-TiN-W interface which shows positional contrast on real samples, see section on *Monte-Carlo Simulation of Interfaces*.

The initial tests were carried out using 4000 electrons per run. Better statistics could be obtained using additional electrons, especially at higher angles where there are generally few electrons scattered, but the overall trends would not be expected to change. Subsequent tests used 50,000 electrons to improve statistics.

Angular Dependency on Beam Voltage

Figure 4 shows the angular dependency of counts for a 100 nm thick silicon sample over a range of beam voltages. Below approx. 2.25 kV no electrons are transmitted through the sample. The count rate tends to zero at 0° due to the vanishing small area over which the flux is applied. The count rate shows a peak at some angle that increases in angle and decreases in value with reducing beam voltage, with the largest peak angle being approx. 600 mrad (35°) before the beam voltage is so low that no electrons are transmitted through the sample at all.

In the literature there are some models for how to consider the angular count rate for transmitted electrons (see for example, [10]). This model uses a single parameter to describe the overall shape of the count rate with a function: exp(-b.sin(θ)).cos(θ).sin(θ). Applying such a model to the current data has not been investigated in detail.

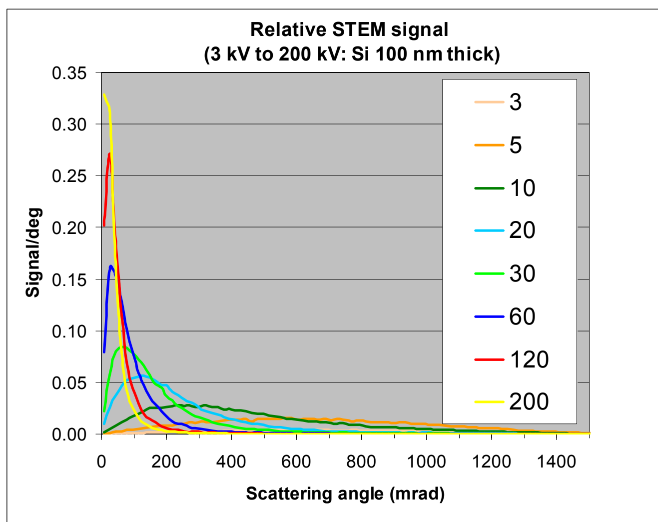

Figure 4: Number of electron counts into 1° wide annular rings for a range of electron voltages from 3 to 200 kV into 100 nm thick silicon.

Comparing Monte Carlo data with actual STEM images

Experiments were run on a set of 6 materials using a variety of beam voltages and sample thicknesses for the annular STEM configuration. The results are shown by the "symbols" in Fig. 5. These data points were obtained using 4000 electrons per run and are shown scaled to a range of 50000 in Fig. 5 to match the lines in the figure (which are discussed below).

Overall, the trends are that the bright field signals get larger as the sample thickness is reduced. The ADF and HADF signals are more complicated with a peak occurring at some thickness for each material. This occurs because when the sample is very thin there is little scattering into the dark field regions and at larger thickness the beam does not make it through the material. The peaks in the ADF signal occur at smaller sample thickness than the HADF, which is to be expected as less scattering is needed for electrons to reach the ADF region.

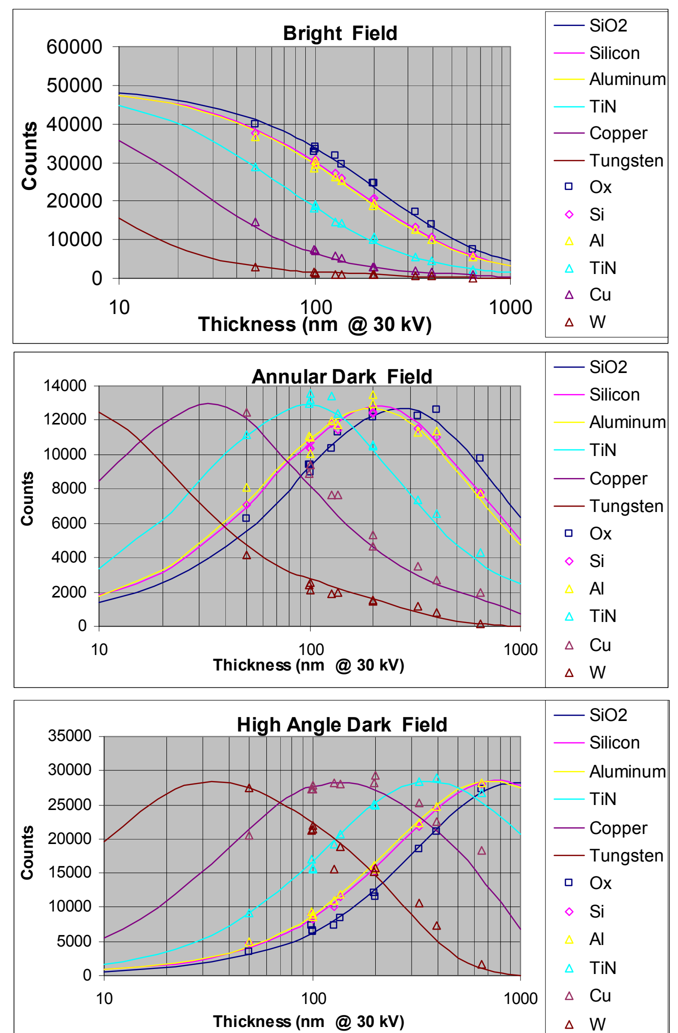

Figure 5: Symbols are results from Monte Carlo experiments. Lines are comparison with the equivalent silicon-kV model (see text).

Figure 6 compares these results to a typical STEM results for BF, ADF and HADF modes. The exact materials making up the ILD (inter-layer dielectric) are not known, but the contrast is expected to be similar to SiO_2. For the three key materials present the images (Fig. 6) and graphs (Fig. 5 at around 100 nm thickness) show similar signal intensity trends:

BF (a): ILD > Si > W
ADF (b): Si > ILD > W
HADF (c): W > Si > ILD

In addition, the ADF image shows the thin TiN layer standing out against both the W and ILD. This again is reflected in the ADF graph, where TiN has the highest signal intensity, and is a common result seen on other samples and demonstrates the value of having multiple STEM signals to choose from to bring out the required sample contrast.

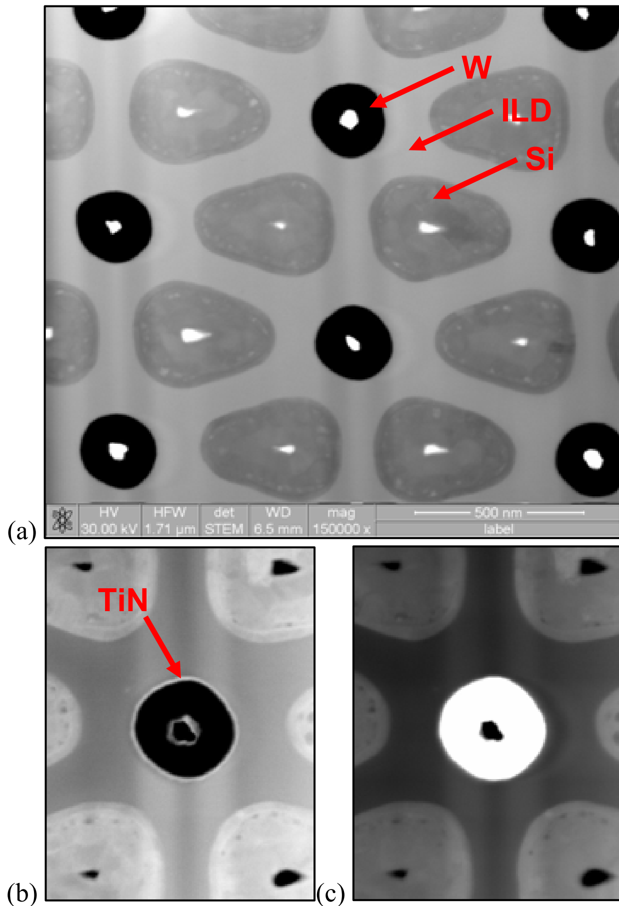

Figure 6: Plan view DRAM sample shown in (a) bright field mode, and zoomed in areas in (b) annular dark field, and (c) high angle dark field modes. The contrast in these images follows that for a ~100nm thick sample shown in Fig. 5, see text for more discussion.

Beam voltage and sample thickness equivalence

When the results shown by the symbols in Fig. 5 were inspected it was noted that very similar counts were obtained for certain combinations of beam voltage and thickness. For example, 100 nm @ 30 kV gave the same result (within the statistical variation seen in Monte Carlo) for BF, ADF and HADF as 50 nm @ 20 kV. This was true for each material and for other thickness-kV combinations.

Overall, for a given material the same counts were obtained when (thickness/$kV^{1.7}$) was constant – Fig. 5 includes values from a variety of kV and thickness plotted at the equivalent thickness for the 30 kV.

This result is consistent with the maximum range model of Kanaya-Okayama (KO) [11].

This model states that:

$$\text{Max range, } R_{KO} = 0.0276.A.E^{1.67} / (D.Z^{0.889}) \qquad \text{[Eq 1]}$$

where, E is in kV and range is in µm

The difference between power factors of 1.67 and 1.7 is well within the statistical error of the modeling, so for the later modeling the kV power of 1.67 from KO range was used for consistency [12].

Some experiments were also carried out with samples tilted into the "STEM while milling" position (tilted by 38° from the top down STEM imaging position). These results were consistent for each material (except for HADF signal for tungsten) with the sample being simply thicker by the amount expected by increasing the thickness by 1/cos(38°). This data is plotted in Fig. 5 as the data at 127 nm (tilt corrected thickness for 100 nm). The poor W correlation for the W signal with HADF is possibly attributed to the large number of multiple scattering events that occur when passing through a tilted layer.

These two results mean that for a combination of sample thickness, tilt and beam voltage is possible to calculate the equivalent sample thickness at 30 kV (or conversely to calculate the equivalent beam voltage for a fixed sample thickness, such as 100 nm). Once this 30 kV thickness is known then the corresponding contrast in the various imaging modes can be predicted from graphs like those in Fig. 5.

Equivalent Si-kV model

Further inspection of the data also showed that for a particular material-kV-thickness combination it was possible to find a beam voltage for a 100 nm thick silicon sample with a similar set of results. If this equivalence could be generalized for any set of sample-beam conditions it would be possible to predict the angular distribution (and hence detector signals) by just knowing the results for silicon over a range of beam voltages.

The first model used the following factor, F:

$$F = (D^d.Z^z/A^a).(t/E^{1.67}) \qquad \text{[Eq 2]}$$

where, d, z, a are model parameters and t is sample thickness

Then using

$$F_{Material} = F_{Silicon} \quad \text{[Eq 3]}$$

for conditions where the angular distribution are the same then it is possible to calculate the equivalent beam voltage E for Si at some standard thickness (in this case 100 nm).

When this model was applied the best parameters to use were found to be:

z=1.0, a=0.5 and d=1.0

It should be noted that for most material A ~ 2.Z and so the factor is not too sensitive to changes in both z and a together – e.g. changing to z=1.1 and a=0.6 gives similar results.

These gave a reasonable agreement between the Monte Carlo values for the 6 materials and that predicted by using the Monte Carlo results from the calculated equivalent beam voltage for silicon. The place where the fit for Eq. 2 was least good was in the HADF signal for W in the range 200 nm and above, where it was seen that the modeled signal dropped off too rapidly compared to the Monte Carlo data for W. Under these conditions the beam energy for silicon is getting close to the cut off voltage where no electrons are transmitted (i.e. R_{KO} is approaching the 100 nm standard sample thickness). To overcome this, the following factor was used:

$$F = (D^d.Z^z/A^a).(t/(E - E_0)^{1.67}) \quad \text{[Eq 4]}$$

Where E_0 is the beam voltage where $t=R_{KO}$ for the material. This does not change the t and E dependency for a given material (due to the way E_0 is dependent upon t), but means that the factor is effectively using the "excess" beam voltage over that needed to get through the sample and have any transmitted electrons at all.

Using this modified factor the fit was better for W over the full thickness range. The parameters that gave the best fit to the data (see Fig. 5) are:

z=1.9, a=1.0 and d=1.0

The fitting to these values was done in an empirical way and a better fit could be investigated using a more analytical method. For this it would probably be necessary to acquire more Monte Carlo data on the various materials using greater numbers of electrons to improve the statistical variation that's seen in such data.

As noted above it is possible to change z and a in sync and get a similar fit to the experimental data. For example, using z=1.4 and a=0.5 is almost as good as the values finally used. The attraction of using z=1.9, a=1.0, d=1.0 is that these are very similar to the factors in the KO equation with an additional Z factor (0.889 + 1 ~ 1.9), which simplifies Eq. 4 to:

$$F = Z / ((R_{KO}/t)^{1/1.67} - 1)^{1.67} \quad \text{[Eq 5]}$$

Equivalent Si-kV Model Results

With this model in place we can now investigate a wider range of sample conditions without having to perform further Monte-Carlo modeling.

Table 1 list some of the materials investigated. They are arranged in order of increasing value of the parameter $[D^d.Z^z/A^a]$, which we'll refer to as the DZ/A factor. This factor is the key value in determining the curve shape (although R_{KO} is also a consideration), so other materials could be estimated simply by looking at an already plotted value with a similar DZ/A value.

Table 1: DZ/A factors for a variety of materials commonly found in semiconductor samples (see text for more details).

Material	Elements	Color	Factor
Low-k Dielectric	SiOC		5.9
Dielectric	SiCN		8.3
Oxide	SiO2		9.9
Silicon / Poly-Si	Si		12.5
Nitride	Si3N4		14.0
Silicon Germanium	SiGe		23.1
Silicide	NiSi		44.5
W-Barrier	TiN		43.6
Copper	Cu		84.5
Cu-Barrier	TaN		247.7
Tungsten	W		373.8

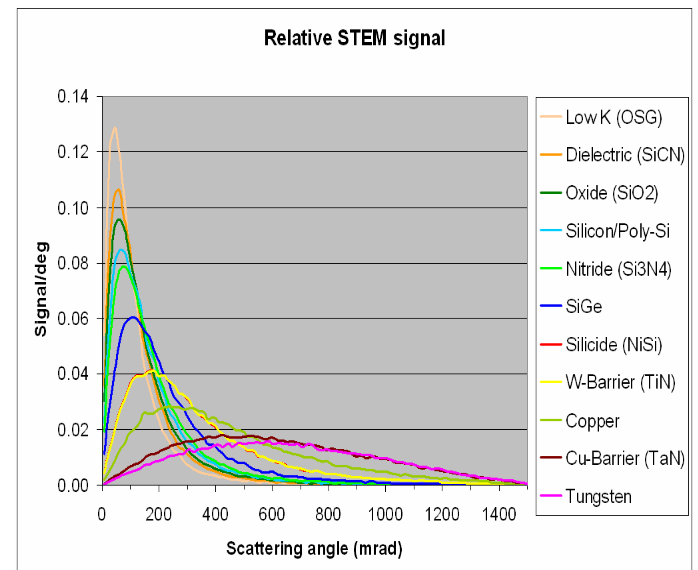

Figure 7: Modeled 30 kV STEM signal as a function of scattering angle for a variety of materials found in semiconductor devices (100 nm sample thickness).

Figure 7 shows an example of the modeled relative STEM signal against scattering angle for the materials in Table 1. By summing the angles that correspond to each region of the STEM detector, the contrast within the different detector modes can be predicted.

Such modeling can help interpret the contrast seen within the SEM-STEM images and help optimize sample preparation and imaging conditions. To compare the modeling to actual STEM images, the regions of different materials in a sample were identified. Figure 8 shows a bright field STEM image whose left half has been overlaid with colored regions to represent the different materials thought present. The upper set of images in Fig. 9 show STEM results from three imaging modes, whilst the lower set shows the corresponding modeled images. In each modeled image the overlay has been replaced by the appropriate grayscale value for the particular imaging mode, showing an excellent correspondence to the original.

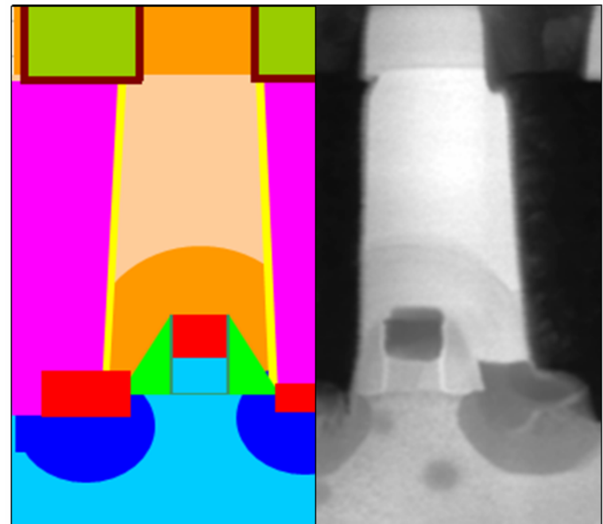

Figure 8: Bright field STEM image whose left half has been overlaid with colored regions that represent the different materials thought present. The overlay colors of the materials match those in shown in Table 1 and Fig. 7.

Monte-Carlo Simulation of Interfaces

In addition to looking at materials in isolation, the simulation of interfaces was also carried out using the Monte-Carlo program. Figure 10 shows a summary of such a result. The 100 nm thick sample consists of a SiO_2 – TiN – W sandwich, the TiN layer being 10 nm wide (shown schematically by the blue stripe in the figure). The electron beam was scanned in 1 nm steps across this interface (assuming a zero dimension electron beam).

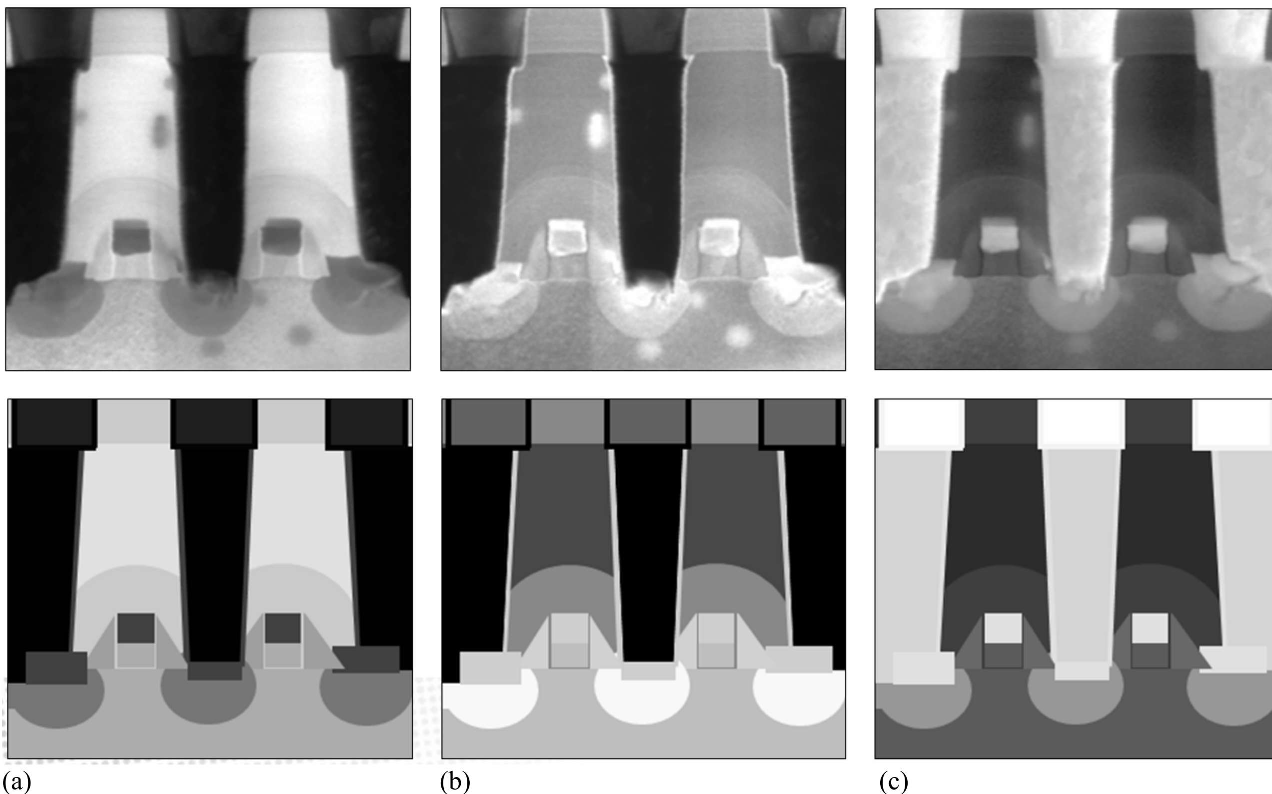

Figure 9: Comparison of actual 30 kV STEM images (upper set) with predicted images based on the STEM modeling (lower set), using the colored regions shown in Fig. 8 to represent each material. The image pairs are (a) bright field, (b) annular dark field and (c) high-angle dark field (partial field).

The results match the modeled images already considered for the cases of bright field and annular dark field – the bright field signal (green) is brighter in the oxide and then drops off to a low level in the Tungsten; while annular dark field signal (yellow) has a peak in the TiN film.

There is a new effect shown by the HADF signal (red line and symbols). The behavior at the interface is more complicated than it would be without the interface present. Now a peak is seen (red line) near the interface before the signal levels off approximately 30 nm from the TiN-W interface. By investigating the azimuthal annular distribution of the transmitted signal this peak can be explained. The HADF transmitted signal was considered for the two halves of the detector – the left half of the detector shown as HADF-1 and the right half as HADF-2. HADF-1 shows a high peak just inside the W layer, while HADF-2 shows much lower signal in this region.

This behavior is attributed to how the scattering occurs within the W layer. Multiple scattering events will occur within the dense W layer and so if any of these result in an electron scattering out of the W and into the TiN/Oxide region then there is a higher probability that it will eventually make its way out of the sample and reach the detector than would be the case of an electron scattering in the opposite direction and had more scattering events in the W layer. Therefore, the half of the HADF on the oxide side of the sample will see increased signal, while the other side sees a reduced one.

This effect can be seen in Fig. 9c where it can be noted that the right side of the W-contacts show enhanced signal in HADF mode towards the detector, which is in partial field mode with half of the segments active.

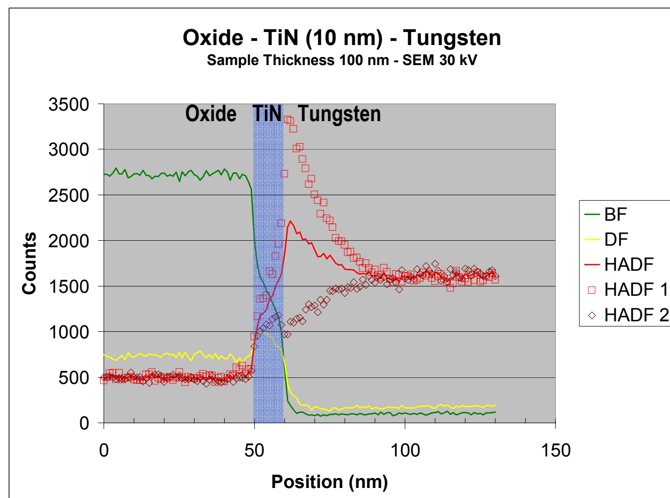

Figure 10: Monte-Carlo simulation of oxide-TiN-tungsten interface. TiN layer is 10 nm thick, sandwiched between the oxide and tungsten regions. The electron beam was stepped by 1 nm per pixel, with a total of 4000 electrons used per point.

Endpoint Monitoring during Sample Thinning

The final example to be discussed is the use of the STEM-model for endpoint monitoring. One application of the Flipstage-STEM combination for endpoint monitoring has already been discussed previously [5]. That method relied on the user viewing the change in apparent feature dimensions as the sample was thinned.

In addition to watching features as they are thinned or eliminated from the image, the transmitted signal (image contrast) will change as the sample is thinned in a predictable way based on the detector geometry in use and beam voltage, sample tilt etc. Therefore, by monitoring the transmitted signal we can get a direct measurement of the thickness via the modeled data. Figure 11 shows such a result, where the STEM signal was monitored in two locations (labeled 1 and 2 in Fig. 12).

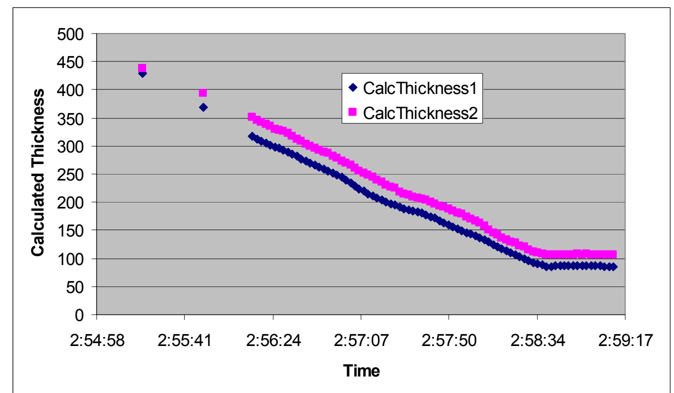

Figure 11: Thinning result from sample monitoring – lines 1 and 2 refer to the locations shown in Fig. 12.

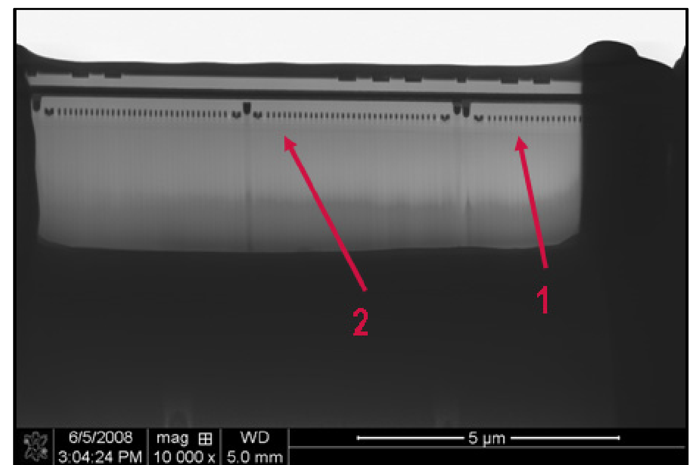

Figure 12: Bright field STEM image at the end of the thinning process depicted in Fig. 11.

In addition to direct monitoring of the sample thickness such a method can also show the angle between locations (Fig. 13) – knowing that an included angle of, in this case, 0.3° is being created will allow the operator to make a small scan rotation

change to the FIB to make the sample more parallel. Similar measurements can also be made in the vertical direction to check for sample uniformity in that direction too.

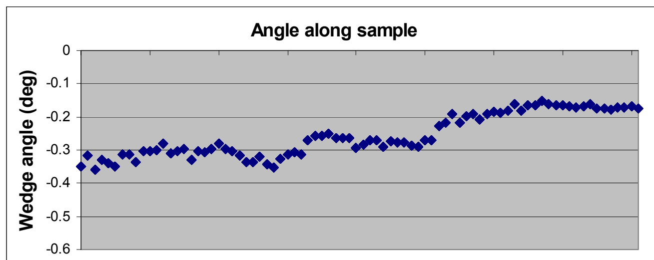

Figure 13: Angle measured along the width of the membrane during thinning, measured between points 1 and 2 in Figs. 11 and 12. X-axis is time, corresponding to the region between approx. 2.56:00 and 2.59:17 in Fig. 11, where data is collected every ~2s.

Conclusions

Modeling of SEM-STEM imaging has been undertaken to understand better the expected contrast in the different STEM modes and how they change with imaging conditions, such as, sample thickness, electron beam voltage and different material parameters. A generalized method has been proposed to relate materials back to a silicon standard sample, enabling new materials to be quickly investigated without doing a full Monte-Carlo simulation. Such modeling can help interpret the contrast seen within the SEM-STEM images and help optimize sample preparation and imaging conditions.

Acknowledgments

Jiang Huang and Pat Harper of Micron Technology Inc, Boise, Idaho are acknowledged their work on the thickness monitoring samples, as are FEI NanoPorts in the US and Europe for images used in this paper.

References

[1] Ma, Z. *et al*, *Microscopy and Microanalysis, proceedings, vol. 5, supplement 2* (1999), pp. 904-905

[2] Xu, Y. *et al*, "Precision TEM Specimen Preparation for Integrated Circuits using Dual-Beam FIB Lift-Out Technique", *Microscopy and Microanalysis proc., vol. 6, supplement 2* (2000), pp. 516-517

[3] Young, R.J., and Moore, M.V., "Dual-beam (FIB/SEM) Systems" in Introduction to Focused Ion Beams: Instrumentation, Theory, Techniques, and Practice, eds. L.A. Giannuzzi and F.A. Stevie, Springer (New York 2004), pp. 247-280

[4] Moore, M.V., "Using in situ STEM to increase resolution in a FIB-SEM," *SCANNING, Vol. 25, May/June 2003*, pp. 159-160

[5] Young, R.J. et al., "In-situ Sample Preparation and High-Resolution SEM-STEM Analysis," *Proc 30th International Symposium for Testing and Failure Analysis*, November 2004, pp. 331-337

[6] Young, R.J., "Three-Dimensional Materials Characterization using Focused Ion Beams (FIB)," Presented at *47th International AVS Symposium*, Boston, MA, October 2000

[7] Vanderlinde, W.J., "STEM (scanning transmission electron microscopy) in a SEM (scanning electron microscope) for Failure Analysis and Metrology", *Proc 28th International Symposium for Testing and Failure Analysis*, November 2002, pp. 77-85

[8] Coyne, E., "A Working Method for adapting the (SEM) Scanning Electron Microscope to Produce (STEM) Scanning Transmission Electron Microscope Images", *Proc 28th International Symposium for Testing and Failure Analysis*, November 2002, pp. 93-99

[9] MC-SET: www.mc-set.com (version 3J22)

[10] Klein et al., "New Expressions for Angular Distributions", *Scanning* 18 (1996), pp.417-427

[11] Kanaya, K. and Okayama, S. "Penetration and energy-loss theory of electrons in solid targets" *J. Phys. D: Appl. Phys. 5* (1972), pp43-58

[12] Private communication: thanks to Milos Toth, FEI Company, Hillsboro, Oregon for first pointing out this relationship to the KO model